

Atomic-Layer-Controlled Magnetic Orders in MnBi₂Te₄-Bi₂Te₃ Topological Heterostructures

Xiong Yao^{1, 2, #, *}, Qirui Cui^{1, 3, #, †}, Zengle Huang⁴, Xiaoyu Yuan⁴, Hee Taek Yi⁴, Deepti Jain⁴,
Kim Kisslinger⁵, Myung-Geun Han⁶, Weida Wu⁴, Hongxin Yang^{3, *}, and Seongshik Oh^{2, *}

¹Ningbo Institute of Materials Technology and Engineering, Chinese Academy of Sciences,
Ningbo 315201, China

²Center for Quantum Materials Synthesis and Department of Physics & Astronomy, Rutgers, The
State University of New Jersey, Piscataway, New Jersey 08854, United States

³Center for Quantum Matter, School of Physics, Zhejiang University, Hangzhou 310058, China

⁴Department of Physics & Astronomy, Rutgers, The State University of New Jersey, Piscataway,
New Jersey 08854, United States

⁵Center for Functional Nanomaterials, Brookhaven National Laboratory, Upton, New York
11973, United States

⁶Condensed Matter Physics and Materials Science, Brookhaven National Laboratory, Upton,
New York 11973, United States

[#]Xiong Yao and Qirui Cui contributed equally to this work.

†Present address: Department of Applied Physics, School of Engineering Sciences, KTH Royal
Institute of Technology, AlbaNova University Center, 10691 Stockholm, Sweden

Email: yaoxiong@nimte.ac.cn, hongxin.yang@zju.edu.cn, ohsean@physics.rutgers.edu

ABSTRACT

The natural van der Waals superlattice $\text{MnBi}_2\text{Te}_4\text{-(Bi}_2\text{Te}_3)_m$ provides an optimal platform to combine topology and magnetism in one system with minimal structural disorder. Here, we show that this system can harbor both ferromagnetic (FM) and antiferromagnetic (AFM) orders and that these magnetic orders can be controlled in two different ways by either varying the Mn-Mn distance while keeping the $\text{Bi}_2\text{Te}_3/\text{MnBi}_2\text{Te}_4$ ratio constant or vice versa. We achieve this by creating atomically engineered sandwich structures composed of Bi_2Te_3 and MnBi_2Te_4 layers. We show that the AFM order is exclusively determined by the Mn-Mn distance whereas the FM order depends only on the overall $\text{Bi}_2\text{Te}_3/\text{MnBi}_2\text{Te}_4$ ratio regardless of the distance between the MnBi_2Te_4 layers. Our results shed light on the origins of the AFM and FM orders and provide insights into how to manipulate magnetic orders not only for the $\text{MnBi}_2\text{Te}_4\text{-Bi}_2\text{Te}_3$ system but also for other magneto-topological materials.

Keywords: Magnetic topological insulator, Interlayer coupling, MnBi_2Te_4 , Tunable magnetism

Intrinsic magnetic topological insulators (MTIs) such as the $\text{MnBi}_2\text{Te}_4\text{-(Bi}_2\text{Te}_3)_m$ ($m = 0, 1, 2, \dots$) compounds, which are composed of a natural stacking of stoichiometric van der Waals units, incorporate topological states and magnetism in a manner that introduces significantly less structural disorder than magnetic doping¹⁻¹⁸. The experimental demonstration of quantum anomalous Hall effect (QAHE) and robust axion insulator state in the MnBi_2Te_4 compound^{2, 3, 19} highlights its potentials for topological spintronics. The MnBi_2Te_4 layers are ferromagnetically coupled within each septuple layer (SL) and antiferromagnetically coupled between SLs in A-type configuration²⁰.

In the $\text{MnBi}_2\text{Te}_4\text{-(Bi}_2\text{Te}_3)_m$ bulk crystals, the antiferromagnetic (AFM) interlayer coupling becomes weaker and eventually turns into ferromagnetic (FM) as non-magnetic Bi_2Te_3 quintuple layers (QLs) are intercalated between the MnBi_2Te_4 layers²¹⁻²⁴. Along this line, people successfully synthesized MnBi_4Te_7 (i.e. $m = 1$), $\text{MnBi}_6\text{Te}_{10}$ ($m = 2$) and $\text{MnBi}_8\text{Te}_{13}$ ($m = 3$) bulk crystals and found coexistence of AFM and FM orders for $m = 1$ and 2 but FM phase for $m = 3$ ^{21-23, 25, 26}, as summarized in Figure 1a. However, introduction of the Bi_2Te_3 extra spacer layers in the $\text{MnBi}_2\text{Te}_4\text{-(Bi}_2\text{Te}_3)_m$ system increases not only the interlayer distance between the two neighboring MnBi_2Te_4 layers (Mn-Mn distance) but also the $\text{Bi}_2\text{Te}_3/\text{MnBi}_2\text{Te}_4$ ratio. The latter effect, which dilutes the overall magnetic ion concentration, possibly plays a non-negligible role in the evolution of magnetic orders, just like the Cr concentration-dependent magnetism in Cr-doped $(\text{Bi,Sb})_2\text{Te}_3$ ²⁷⁻²⁹. Accordingly, the exact role of $\text{Bi}_2\text{Te}_3/\text{MnBi}_2\text{Te}_4$ ratio apart from the influence of Mn-Mn distance in these $\text{MnBi}_2\text{Te}_4\text{-(Bi}_2\text{Te}_3)_m$ compounds is unclear²¹⁻²⁴. Moreover, with the superlattice structure in these bulk crystals, it would not be possible to independently control Mn-Mn distance and $\text{Bi}_2\text{Te}_3/\text{MnBi}_2\text{Te}_4$ ratio. On the other hand, recent studies report that magnetic defects such as Mn antisites can induce ferromagnetism in bulk crystals of MnBi_4Te_7 , $\text{MnBi}_6\text{Te}_{10}$, and

MnSb_2Te_4 ³⁰⁻³⁸, the sister compound of MnBi_2Te_4 . In order to precisely engineer the magnetic properties in such complex magneto-topological materials, clear understanding of all these effects, especially the exact roles of $\text{Bi}_2\text{Te}_3/\text{MnBi}_2\text{Te}_4$ ratio and the Mn-Mn distance, is essential. The layer-by-layer molecular beam epitaxy (MBE) technique allows us to independently control those two effects at atomic level through an artificial layering scheme³⁹, providing a strategy to disentangle Mn-Mn distance and $\text{Bi}_2\text{Te}_3/\text{MnBi}_2\text{Te}_4$ ratio regarding their effects on the magnetic orders (both AFM and FM) in this system, which has never been explored previously.

Independent Control of $\text{Bi}_2\text{Te}_3/\text{MnBi}_2\text{Te}_4$ ratio and Mn-Mn distance. In order to investigate the effect of Mn-Mn distance and $\text{Bi}_2\text{Te}_3/\text{MnBi}_2\text{Te}_4$ ratio on the magnetic properties of the $\text{MnBi}_2\text{Te}_4\text{-Bi}_2\text{Te}_3$ heterostructures separately, we designed and grew two sets of $\text{MnBi}_2\text{Te}_4\text{-Bi}_2\text{Te}_3$ heterostructures (Figure 1b and c), using our atomic-layer-by-layer molecular beam epitaxy (MBE) technique^{10, 38, 40-44}. In configuration (b), we added n QL Bi_2Te_3 layers on each side of a single slab of $\text{MnBi}_2\text{Te}_4\text{-Bi}_2\text{Te}_3\text{-MnBi}_2\text{Te}_4$ structure while keep the Mn-Mn distance constant. On the other hand, in configuration (c), the $\text{Bi}_2\text{Te}_3/\text{MnBi}_2\text{Te}_4$ ratio (total Bi_2Te_3 thickness) is fixed while the Mn-Mn distance is varied. It is important to note that all these samples are not a superlattice (which is a repetition of a unit cell structure), and rather they are a single slab heterostructure. As shown in Figure 1d, we achieved independent control of $\text{Bi}_2\text{Te}_3/\text{MnBi}_2\text{Te}_4$ ratio and the Mn-Mn distance in configuration (b) and (c), respectively, while both of these two effects vary together in the $\text{MnBi}_2\text{Te}_4\text{-(Bi}_2\text{Te}_3)_m$ bulk crystals (which are in superlattice structure). Figure 1e shows the typical high-angle annular dark-field scanning transmission electron microscopy (HAADF-STEM) image of a $\text{MnBi}_2\text{Te}_4\text{-Bi}_2\text{Te}_3$ heterostructure, which exhibits well-defined QL and SL structures of Bi_2Te_3 and MnBi_2Te_4 layers, respectively, with sharp van der Waals gaps between two adjacent layers. The sample quality was further confirmed by reflection high-energy

electron diffraction (RHEED) patterns, as shown in Figure S1. It is notable that despite the well-defined QL and SL structures, stacking of MnBi_2Te_4 and Bi_2Te_3 layers is inherently non-uniform at the macroscopic scale for all MBE-grown films. Nonetheless, since transport measurements reflect the average properties of the entire sample and all our samples were grown under identical conditions, the non-uniform stacking is neither a variable factor in our study nor does it impact the conclusions in the subsequent sections.

The origin of coexisting AFM and FM orders. We found that AFM and FM orders coexist in many of our MnBi_2Te_4 - Bi_2Te_3 heterostructures as shown in Figures 3 and 4. So, first, we investigate their origin in Figure 2, by combining scanning tunneling microscopy (STM) and first principles calculations. Previously it was reported that magnetic defects like Mn antisites or Mn-Bi site mixing can enhance FM order in MnSb_2Te_4 , MnBi_4Te_7 and $\text{MnBi}_6\text{Te}_{10}$ ³⁰⁻³⁴. To determine the distribution of magnetic defects in our samples, we mapped out the Mn_{Bi} antisite defects in the $n = 0$ sample (configuration (b)) by STM, as shown in Figure 2a. The Mn_{Bi} antisites appear as dark defects in the marked triangles. The density of Mn_{Bi} antisites are determined as 2.1% on average by counting the defects in the measured region in Figure 2a. On the other hand, for $n = 4$ (Figure 2b), the Mn density ($\sim 0.2\%$) is ten times smaller than the value in Figure 2a, strongly suggesting that the Mn_{Bi} antisite defects are mostly confined within the MnBi_2Te_4 layer and the interlayer Mn diffusion is minuscule compared with the Mn density in the MnBi_2Te_4 layer.

To give a further insight into the relationship between Mn_{Bi} magnetic defects and the FM order, we conducted first-principles calculations of the MnBi_2Te_4 - Bi_2Te_3 heterostructure where some Bi atoms are substituted by Mn atoms for simulating Mn_{Bi} defects, as shown in the left panel of Figure 2c. The ground state of the MnBi_2Te_4 - Bi_2Te_3 heterostructure without Mn antisite defects was determined as AFM (right panel of Figure 2c). However, as more Bi sites are replaced by Mn

atoms, the energy difference between AFM and FM coupling quickly narrows to nearly 0 at the critical Mn doping level of 3.57%, and FM coupling becomes the ground state, then reaching its peak strength at 7.14% of Mn before decreasing with further Mn. It is worth noting that the AFM coupling would become the ground state again above 14.28% of Mn doping according to the trend in Figure 2c, which is consistent with the observations in MnTe intercalated MnBi_2Te_4 superlattices⁴¹. Even though Figure 2c only gives one possible configuration for Mn substitution, this suggests that the magnetic ground state can be easily switched between AFM and FM state depending on the level of Mn defect densities. As observed in Figure 2a, the distribution of Mn defect concentration is inhomogeneous in our films, suggesting that the Mn defect density could be lower than the critical density of AFM-to-FM transition at Mn poor regions but higher than that value at Mn clustered regions. In other words, inhomogeneous Mn defect densities can naturally explain the coexistence of FM and AFM orders in our MnBi_2Te_4 - Bi_2Te_3 heterostructures.

The effect of $\text{Bi}_2\text{Te}_3/\text{MnBi}_2\text{Te}_4$ ratio on AFM and FM orders. In configuration (b), the top and bottom n QL Bi_2Te_3 layers increase only the $\text{Bi}_2\text{Te}_3/\text{MnBi}_2\text{Te}_4$ ratio, while the Mn-Mn distance is fixed. To investigate the exact role of these outer extension layers, we performed systematic longitudinal and Hall resistance measurements on samples with varying n values. Figure 3a exhibits the corresponding magnetic-field-dependent longitudinal resistance for all the samples measured at 2 K. There are several peculiar features in Figure 3a. First, in samples $n = 0, 1, \text{ and } 2$, we can clearly observe two symmetric shoulder peaks at around 3 T. This shoulder feature is commonly observed in MnBi_2Te_4 and is related to magnetic-field-driven spin-flopping process in antiferromagnet³, suggesting the presence of AFM order. As marked by the dash lines in Figure 3a, the spin-flop magnetic field remains unchanged for samples $n = 0, 1 \text{ and } 2$, implying the energy scale or strength of AFM order remains unaffected by increasing n values. The intensity of the

shoulder features gradually reduces as n increases and then completely vanishes in samples $n = 3, 4$ and 5 , likely due to the smearing effect from increased conduction contribution of additional Bi_2Te_3 extension layers. Second, all the curves exhibit clear negative magnetoresistance (MR) peaks around zero field with hysteresis in samples $n = 0$ to $n = 4$ (shown in Figure S2), which are generally observed in various FM materials and regarded as features of FM order^{2, 40, 45}. Figure S2 gives the enlarged plot of Figure 3a at low magnetic fields. With increasing Bi_2Te_3 extension layers, the characteristic magnetic field of FM hysteresis peaks gradually reduces and eventually approaches zero, indicating weakening FM order.

Hall resistance is another probe to detect the magnetic signatures in thin film samples. Figure 3b presents the temperature-dependent Hall resistance measured under zero magnetic field while cooling down for all the samples. All the R_{xy} vs T curves show clear transitions at low temperatures, which is direct evidence of spontaneous magnetization induced by FM order. The transition temperatures show a monotonic decrease with increasing n values, implying reduced FM order. We conducted Hall resistance loop measurements on all the samples at 2 K, as shown in Figure 3c. Notably, they all exhibit clear hysteresis loops, indicating net magnetization resulting from ferromagnetism. As the number of Bi_2Te_3 extension layers n increases, the size of hysteresis loops monotonically shrinks in Figure 3c, reflecting weakening FM order. The coercive fields H_C and the magnetic transition temperature T_C follow very similar trend with increasing n values as shown in Figure 3d, suggesting that both quantities originate from the same (FM) origin. Summarizing the results of Figure 3, we can conclude that AFM and FM orders coexist in these samples and that the added Bi_2Te_3 extension layers, which increase the $\text{Bi}_2\text{Te}_3/\text{MnBi}_2\text{Te}_4$ ratio, significantly weakens FM order while keeping AFM order almost unaffected.

The effect of Mn-Mn distance on AFM and FM orders. In order to see how the Mn-Mn distance alone affects the AFM and FM orders, we implemented heterostructures in configuration (c) (as shown in Figure 1c and Figure 4a): this keeps the $\text{Bi}_2\text{Te}_3/\text{MnBi}_2\text{Te}_4$ ratio (also the overall composition) the same as that of the “ $n = 3$ ” sample in Figure 1b. The corresponding longitudinal and Hall resistance are shown in Figure 4b-e. Interestingly, from Figure 4e we find that the spin-flop feature at around 3 T in the R_{xx} vs $\mu_0 H$ data, characteristic of the AFM order in Figure 3a, emerges when the Mn-Mn distance is reduced to “ $d = 0$ ” from “ $d = 1$ ” but disappears as the Mn-Mn distance increases. It is worth to mention that the vanishing spin-flop feature here are not likely due to the smearing effect from Bi_2Te_3 layers, as the total thickness of Bi_2Te_3 (also the conduction contribution from Bi_2Te_3) are fixed for all the samples in Figure 4a. This observation indicates that the AFM interlayer coupling in $d = 0$ is stronger than other samples, owing to the absence of Bi_2Te_3 spacer layers in the middle. Previous studies on $\text{MnBi}_2\text{Te}_4-(\text{Bi}_2\text{Te}_3)_m$ bulk crystals also suggest that the AFM order can be controlled by Bi_2Te_3 spacer layers, as illustrated by the decreasing T_N in Figure 1a^{21, 22, 24}. However, in the superlattice-like bulk crystal case, the effect of Mn-Mn distance is mixed with the impact of variable $\text{Bi}_2\text{Te}_3/\text{MnBi}_2\text{Te}_4$ ratio. Now we clarify that the Mn-Mn distance plays a dominating role in manipulating the AFM order in $\text{MnBi}_2\text{Te}_4\text{-Bi}_2\text{Te}_3$ systems, disentangling these two effects through the atomic-layer-controlled MBE growth, in a single-slab configuration.

On the other hand, Figures 4b-d show that the strength of FM order, as measured by H_C and T_C , remains little affected by the Mn-Mn distance. With increasing Mn-Mn distance, the variation of both H_C and T_C are limited to fluctuation level and not exhibiting any observable trend. Such behavior is also in stark contrast with the observations in $(\text{Cr,Bi,Sb})_2\text{Te}_3$ system, where the FM order is highly tunable with non-magnetic spacers even if the total composition is fixed⁴⁰, implying

that the ferromagnetism in these two typical MTI materials, $\text{MnBi}_2\text{Te}_4\text{-Bi}_2\text{Te}_3$ and $(\text{Cr,Bi,Sb})_2\text{Te}_3$, are driven by different factors. Combining the observations in Figures 3 and 4 leads to the conclusion that while AFM order is sensitive to the Mn-Mn distance, the FM order is not, but instead, mostly dominated by the overall $\text{Bi}_2\text{Te}_3/\text{MnBi}_2\text{Te}_4$ ratio. It is worth mentioning that magnetic disorder⁴⁶, which can cause a spatial variation in magnetic exchange gap, could become more pronounced with increasing Mn-Mn distance due to reduced interlayer coupling. Accordingly, weakening AFM order with increasing Mn-Mn distance is likely to be a combined result of reduced exchange coupling and enhanced magnetic disorder. On the other hand, considering that magnetic defects tend to promote the FM order as shown in Figure 2c, FM order is less likely to be affected by magnetic disorder in this system. The contrasting response behavior of AFM and FM orders to various effects provide valuable insights into designing novel MTI heterostructure materials.

In summary, we observed coexisting AFM and FM orders in the $\text{MnBi}_2\text{Te}_4\text{-Bi}_2\text{Te}_3$ heterostructures, which originate from the presence of Mn_{Bi} antisite defects. Through transport measurements, we unveiled that in this system, the increased $\text{Bi}_2\text{Te}_3/\text{MnBi}_2\text{Te}_4$ ratio suppresses FM order even when the Mn-Mn interlayer distance is kept constant, whereas the AFM order is almost exclusively determined by the Mn-Mn interlayer distance. This observation strongly suggests that in the $\text{MnBi}_2\text{Te}_4\text{-Bi}_2\text{Te}_3$ system, the AFM order originates from direct interlayer coupling between the neighboring Mn ions whereas the FM order depends only on the overall $\text{Bi}_2\text{Te}_3/\text{MnBi}_2\text{Te}_4$ ratio regardless of the distance between the MnBi_2Te_4 layers. These results reveal the complex interplay between magnetic coupling, Mn-Mn interlayer distance, and $\text{Bi}_2\text{Te}_3/\text{MnBi}_2\text{Te}_4$ ratio in the $\text{MnBi}_2\text{Te}_4\text{-Bi}_2\text{Te}_3$ heterostructures. In particular, our work demonstrates that the atomic-layer-engineering can be used as an effective tool to control the

magnetic orders in topological $\text{MnBi}_2\text{Te}_4\text{-Bi}_2\text{Te}_3$ heterostructures, toward novel magneto-topological effects.

EXPERIMENTAL SECTION

Sample Preparation. We grew all the $\text{MnBi}_2\text{Te}_4\text{-Bi}_2\text{Te}_3$ heterostructures on $10 \times 10 \text{ mm}^2$ Al_2O_3 (0001) substrates using a custom-built MBE system with a base pressure of low 10^{-10} Torr. Substrates were treated by methods reported in our previous works^{8, 9, 40, 47-49}. The MnBi_2Te_4 and Bi_2Te_3 layers were deposited at $300 \text{ }^\circ\text{C}$. Between the deposition of each SL MnBi_2Te_4 or each QL Bi_2Te_3 layer, we annealed the film at $300 \text{ }^\circ\text{C}$ for 1 minute under Te flux. Then Te capping layer was deposited on top after the samples were cooled down to room temperature.

Transport Measurement. All measurements were performed using the standard van der Pauw geometry, by manually pressing four indium wires on the corners of each sample. The transport measurements were performed in a Quantum Design Physical Property Measurement System (PPMS; 2 K). Raw data of R_{xx} and R_{xy} were properly symmetrized and anti-symmetrized.

Computational Methods. We performed first-principles calculations with the Vienna ab initio simulation package (VASP) based on the density functional theory (DFT)⁵⁰⁻⁵². The exchange-correlation functionals are treated by the generalized gradient approximation (GGA) in Perdew-Burke-Ernzerhof (PBE) form⁵³. The cutoff energy of plane wave expansion is set to 420 eV. An $18 \times 18 \times 1$ Γ -center k-point mesh is dense enough for sampling the Brillouin zone. A vacuum space of 15 Å is adopted in periodical direction for avoiding the interactions between adjacent layers. All structures are fully relaxed until Hellmann-Feynman force acting on each atom is less than $10^{-2} \text{ eV}/\text{Å}$, and the convergence criterion of total energy is set to 10^{-6} eV . For describing the strong correlation effects of 3d electrons of Mn, GGA+U method is adopted where the U_{eff} is set to 3 eV. The effect of van der Waals interactions are considered by employing the DFT+D3 method.

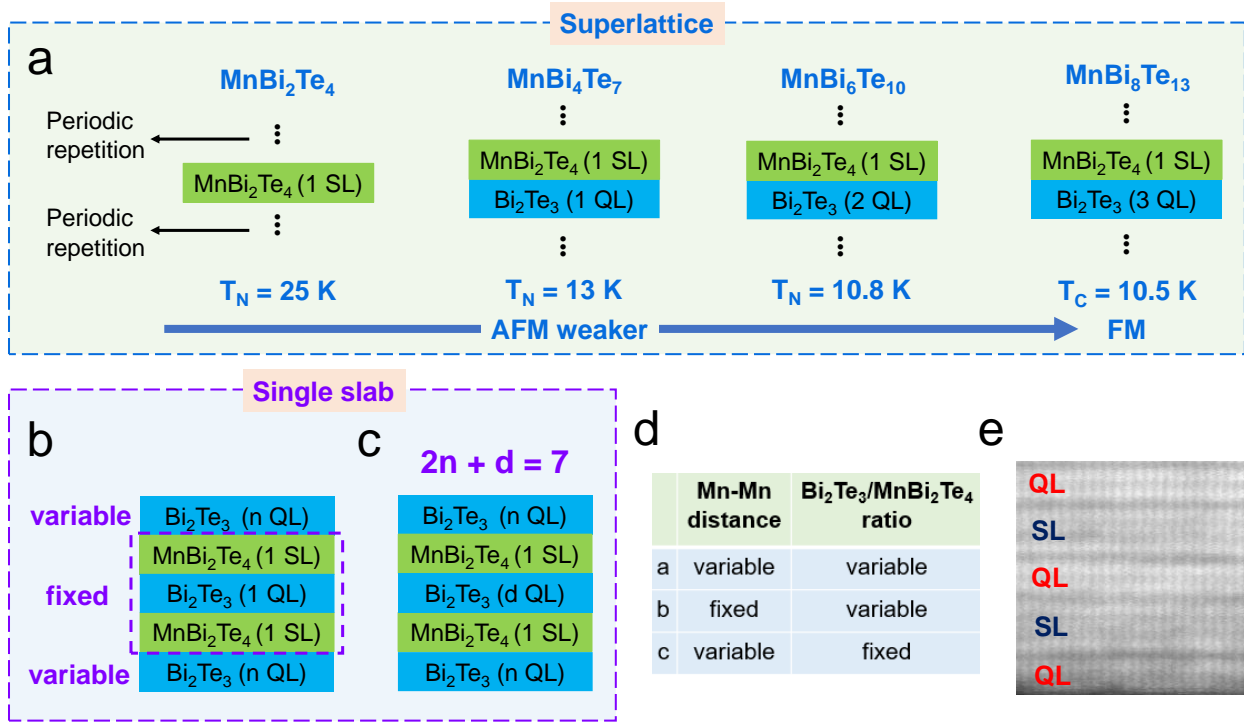


Figure 1. (a) Summary of the studies on $\text{MnBi}_2\text{Te}_4\text{-(Bi}_2\text{Te}_3)_m$ bulk crystal family, results are extracted from Reference 13-16. (b, c) Illustration of the two sets of $\text{MnBi}_2\text{Te}_4\text{-Bi}_2\text{Te}_3$ heterostructures used for the current study. In (b) the n QL Bi_2Te_3 layers are used as extension layers while keeping the Mn-Mn distance constant in the middle layers, while in (c) the total thickness of Bi_2Te_3 is fixed (7 QL) and the spacer Bi_2Te_3 layer is varied. (d) Comparison of the three configurations in (a-c). Notably, configuration (a) is superlattice structure while configurations (b) and (c) are single slab heterostructures. (e) High-angle annular dark-field scanning transmission electron microscopy (HAADF-STEM) image of a typical heterostructure sample. The stacking of MnBi_2Te_4 and Bi_2Te_3 layers are labeled by SL and QL, respectively.

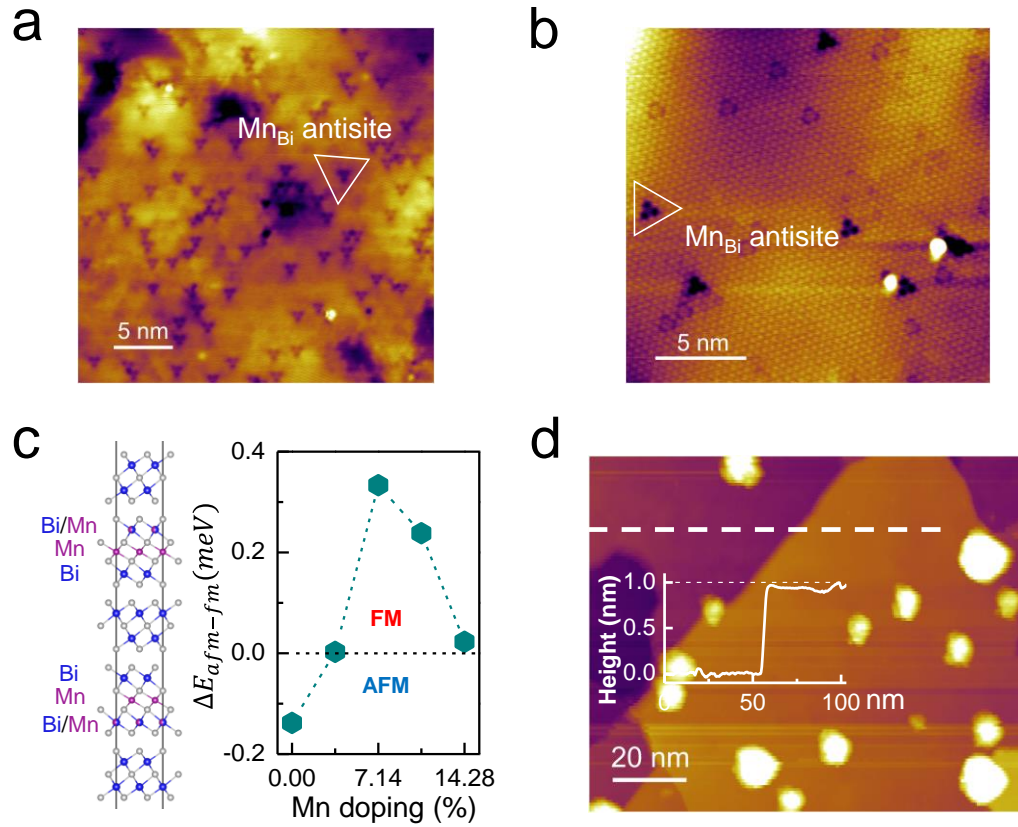


Figure 2. Mn_{Bi} antisite defects toward coexisting FM and AFM orders in the $MnBi_2Te_4$ - Bi_2Te_3 heterostructures. (a, b) Scanning tunneling microscopy (STM) images of the Mn_{Bi} antisites collected at the topmost layer of the $MnBi_2Te_4$ - Bi_2Te_3 heterostructures (configuration (b)) with (a) $n = 0$ and (b) $n = 4$. (c) Left panel is the schematic structure of one possible Mn doping configuration in $MnBi_2Te_4$ - Bi_2Te_3 heterostructures. Right panel shows the Mn-doping-level-dependent energy difference between AFM and FM ground states obtained by first principles calculations. (d) The topography image collected on sample $n = 4$. The inset shows the height profile of terrace with height of around 1 nm, corresponding to the thickness of 1 QL Bi_2Te_3 . The white dots are residual Te from the Te capping layer after decapping process.

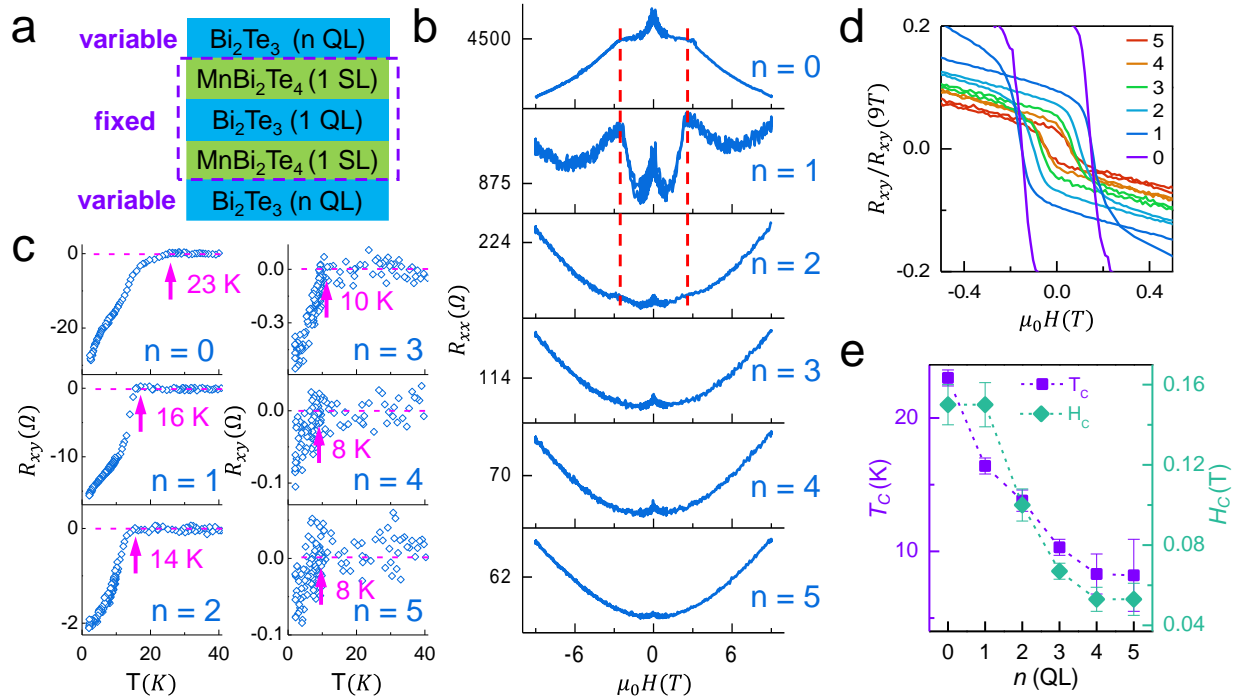


Figure 3. Transport results of the MnBi₂Te₄-Bi₂Te₃ heterostructures with configuration (b) (Figure 1b). (a) Schematic illustration of the MnBi₂Te₄-Bi₂Te₃ heterostructures with fixed Mn-Mn distance while varying Bi₂Te₃/MnBi₂Te₄ ratio. Here “n” refers to the thickness of the outer Bi₂Te₃ layers. (b) Magnetic field-dependent longitudinal sheet resistance of the MnBi₂Te₄-Bi₂Te₃ heterostructures with n values from 0 to 5. (c) Temperature-dependent Hall resistance measured while cooling down under zero magnetic field for all the heterostructure samples. (d) Normalized Hall resistance of the MnBi₂Te₄-Bi₂Te₃ heterostructures with n values from 0 to 5 measured at 2 K. (e) Summary of ferromagnetic transition temperatures T_C determined by (c) and coercive fields H_C determined by (d).

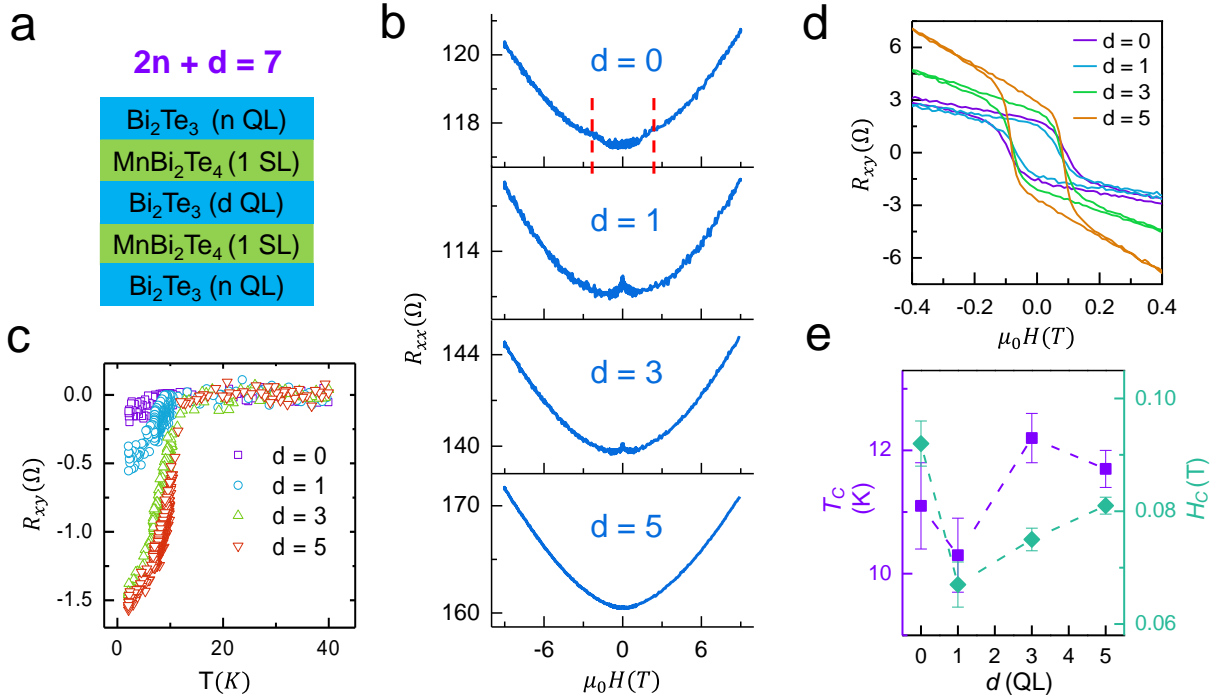


Figure 4. Transport results of the $\text{MnBi}_2\text{Te}_4\text{-Bi}_2\text{Te}_3$ heterostructures with configuration (c) (Figure 1c). (a) Schematic illustration of the $\text{MnBi}_2\text{Te}_4\text{-Bi}_2\text{Te}_3$ heterostructures with fixed $\text{Bi}_2\text{Te}_3/\text{MnBi}_2\text{Te}_4$ ratio while varying Mn-Mn distance. Here “d” refers to the distance between the two MnBi_2Te_4 layers. (b) Magnetic field-dependent longitudinal sheet resistance of the $\text{MnBi}_2\text{Te}_4\text{-Bi}_2\text{Te}_3$ heterostructures with d values from 0 to 5. (c) Hall resistance measured under zero magnetic field for all the heterostructure samples with varying d values. (d) Magnetic-field-dependent Hall resistance of these samples measured at 2 K. (e) Summary of the ferromagnetic transition temperatures and coercive magnetic fields determined from (c) and (d). Note that the shoulder feature at 3 T in the R_{xx} vs μ_0H data, characteristic of the AFM order, appears only in the d = 0 sample, confirming that the AFM order strongly depends on the Mn-Mn interlayer distance. In contrast, the strength of the FM order as measured by H_C and T_C in (e) remains little affected by the Mn-Mn distance.

Supporting information:

The RHEED patterns of the $\text{MnBi}_2\text{Te}_4\text{-Bi}_2\text{Te}_3$ heterostructure, and the longitudinal sheet resistance of the $\text{MnBi}_2\text{Te}_4\text{-Bi}_2\text{Te}_3$ heterostructures.

AUTHOR INFORMATION

Corresponding Authors

*E-mail: yaoxiong@nimte.ac.cn

*E-mail: hongxin.yang@zju.edu.cn

*E-mail: ohsean@physics.rutgers.edu

Author Contributions

X.Yao and S.O. conceived the experiments; X.Yao, X.Yuan, H.T.Y, D.J., and S.O. grew the thin films; X.Yao performed the transport measurements and analyzed the data with Q.C., H.Y. and S.O.; Q.C. and H.Y. performed the first principles calculations; Z.H. and W.W. performed the STM measurements; X.Yao and S.O. wrote the manuscript with contributions from Q.C. and H.Y.

Notes

The authors declare no competing financial interest.

ACKNOWLEDGMENT

The work at Rutgers is supported by Army Research Office's W911NF2010108, MURI W911NF2020166, and the center for Quantum Materials Synthesis (cQMS), funded by the Gordon and Betty Moore Foundation's EPiQS initiative through grant GBMF10104. The work is also

supported by the National Natural Science Foundation of China (Grant No. 12304541) and the Ningbo Science and Technology Bureau (Grant No. 2023J047). The first-principles calculations are supported by the “Pioneer” and “Leading Goose” R&D Program of Zhejiang Province (Grant No. 2022C01053), the National Key Research and Development Program of China (MOST) (Grant No. 2022YFA1405100), the National Natural Science Foundation of China (Grant No. 12174405), Ningbo Key Scientific and Technological Project (Grant No. 2021000215). This research used the Electron Microscopy resources of the Center for Functional Nanomaterials (CFN), which is a U.S. Department of Energy Office of Science User Facility, at Brookhaven National Laboratory under Contract No. DE-SC0012704.

REFERENCES

1. Rienks, E. D. L.; Wimmer, S.; Sanchez-Barriga, J.; Caha, O.; Mandal, P. S.; Ruzicka, J.; Ney, A.; Steiner, H.; Volobuev, V. V.; Groiss, H.; Albu, M.; Kothleitner, G.; Michalicka, J.; Khan, S. A.; Minar, J.; Ebert, H.; Bauer, G.; Freyse, F.; Varykhalov, A.; Rader, O.; Springholz, G. Large magnetic gap at the Dirac point in $\text{Bi}_2\text{Te}_3/\text{MnBi}_2\text{Te}_4$ heterostructures. *Nature* **2019**, *576* (7787), 423-428.
2. Deng, Y.; Yu, Y.; Shi, M. Z.; Guo, Z.; Xu, Z.; Wang, J.; Chen, X. H.; Zhang, Y. Quantum anomalous Hall effect in intrinsic magnetic topological insulator MnBi_2Te_4 . *Science* **2020**, *367* (6480), 895-900.
3. Liu, C.; Wang, Y.; Li, H.; Wu, Y.; Li, Y.; Li, J.; He, K.; Xu, Y.; Zhang, J.; Wang, Y. Robust axion insulator and Chern insulator phases in a two-dimensional antiferromagnetic topological insulator. *Nat. Mater.* **2020**, *19* (5), 522-527.
4. Chen, Y. J.; Xu, L. X.; Li, J. H.; Li, Y. W.; Wang, H. Y.; Zhang, C. F.; Li, H.; Wu, Y.; Liang, A. J.; Chen, C.; Jung, S. W.; Cacho, C.; Mao, Y. H.; Liu, S.; Wang, M. X.; Guo, Y. F.; Xu, Y.; Liu, Z. K.; Yang, L. X.; Chen, Y. L. Topological Electronic Structure and Its Temperature Evolution in Antiferromagnetic Topological Insulator MnBi_2Te_4 . *Physical Review X* **2019**, *9* (4), 041040.
5. Li, J.; Li, Y.; Du, S.; Wang, Z.; Gu, B. L.; Zhang, S. C.; He, K.; Duan, W.; Xu, Y. Intrinsic magnetic topological insulators in van der Waals layered MnBi_2Te_4 -family materials. *Sci. Adv.* **2019**, *5* (6), eaaw5685.
6. Yao, X.; Gao, B.; Han, M. G.; Jain, D.; Moon, J.; Kim, J. W.; Zhu, Y.; Cheong, S. W.; Oh, S. Record High-Proximity-Induced Anomalous Hall Effect in $(\text{Bi}_x\text{Sb}_{1-x})_2\text{Te}_3$ Thin Film Grown on CrGeTe_3 Substrate. *Nano Lett.* **2019**, *19* (7), 4567-4573.

7. Salehi, M.; Yao, X.; Oh, S. From classical to quantum regime of topological surface states via defect engineering. *SciPost Physics Lecture Notes* **2022**, 58.
8. Yao, X.; Yi, H. T.; Jain, D.; Oh, S. Suppressing carrier density in $(\text{Bi}_x\text{Sb}_{1-x})_2\text{Te}_3$ films using Cr_2O_3 interfacial layers. *J. Phys. D: Appl. Phys.* **2021**, 54 (50), 504007.
9. Yi, H. T.; Jain, D.; Yao, X.; Oh, S. Enhanced Quantum Anomalous Hall Effect with an Active Capping Layer. *Nano Lett.* **2023**, 23 (12), 5673-5679.
10. Hirahara, T.; Otrokov, M. M.; Sasaki, T. T.; Sumida, K.; Tomohiro, Y.; Kusaka, S.; Okuyama, Y.; Ichinokura, S.; Kobayashi, M.; Takeda, Y.; Amemiya, K.; Shirasawa, T.; Ideta, S.; Miyamoto, K.; Tanaka, K.; Kuroda, S.; Okuda, T.; Hono, K.; Ereemeev, S. V.; Chulkov, E. V. Fabrication of a novel magnetic topological heterostructure and temperature evolution of its massive Dirac cone. *Nat. Commun.* **2020**, 11 (1), 4821.
11. Tokura, Y.; Yasuda, K.; Tsukazaki, A. Magnetic topological insulators. *Nature Reviews Physics* **2019**, 1 (2), 126-143.
12. Chang, C.-Z.; Liu, C.-X.; MacDonald, A. H. Colloquium: Quantum anomalous Hall effect. *Rev. Mod. Phys.* **2023**, 95 (1), 011002.
13. Hasan, M. Z.; Kane, C. L. Colloquium: Topological insulators. *Rev. Mod. Phys.* **2010**, 82 (4), 3045-3067.
14. Chang, C. Z.; Zhang, J.; Feng, X.; Shen, J.; Zhang, Z.; Guo, M.; Li, K.; Ou, Y.; Wei, P.; Wang, L. L.; Ji, Z. Q.; Feng, Y.; Ji, S.; Chen, X.; Jia, J.; Dai, X.; Fang, Z.; Zhang, S. C.; He, K.; Wang, Y.; Lu, L.; Ma, X. C.; Xue, Q. K. Experimental observation of the quantum anomalous Hall effect in a magnetic topological insulator. *Science* **2013**, 340 (6129), 167-170.

15. Checkelsky, J. G.; Yoshimi, R.; Tsukazaki, A.; Takahashi, K. S.; Kozuka, Y.; Falson, J.; Kawasaki, M.; Tokura, Y. Trajectory of the anomalous Hall effect towards the quantized state in a ferromagnetic topological insulator. *Nat. Phys.* **2014**, 10 (10), 731-736.
16. Kou, X.; Guo, S. T.; Fan, Y.; Pan, L.; Lang, M.; Jiang, Y.; Shao, Q.; Nie, T.; Murata, K.; Tang, J.; Wang, Y.; He, L.; Lee, T. K.; Lee, W. L.; Wang, K. L. Scale-invariant quantum anomalous Hall effect in magnetic topological insulators beyond the two-dimensional limit. *Phys. Rev. Lett.* **2014**, 113 (13), 137201.
17. Jiang, Z.; Chang, C. Z.; Tang, C.; Wei, P.; Moodera, J. S.; Shi, J. Independent Tuning of Electronic Properties and Induced Ferromagnetism in Topological Insulators with Heterostructure Approach. *Nano Lett.* **2015**, 15 (9), 5835-5840.
18. Tang, C.; Chang, C. Z.; Zhao, G.; Liu, Y.; Jiang, Z.; Liu, C. X.; McCartney, M. R.; Smith, D. J.; Chen, T.; Moodera, J. S.; Shi, J. Above 400-K robust perpendicular ferromagnetic phase in a topological insulator. *Sci. Adv.* **2017**, 3 (6), e1700307.
19. Zhang, D.; Shi, M.; Zhu, T.; Xing, D.; Zhang, H.; Wang, J. Topological Axion States in the Magnetic Insulator MnBi_2Te_4 with the Quantized Magnetoelectric Effect. *Phys. Rev. Lett.* **2019**, 122 (20), 206401.
20. Sass, P. M.; Kim, J.; Vanderbilt, D.; Yan, J.; Wu, W. Robust A-Type Order and Spin-Flop Transition on the Surface of the Antiferromagnetic Topological Insulator MnBi_2Te_4 . *Phys. Rev. Lett.* **2020**, 125 (3), 037201.
21. Hu, C.; Gordon, K. N.; Liu, P.; Liu, J.; Zhou, X.; Hao, P.; Narayan, D.; Emmanouilidou, E.; Sun, H.; Liu, Y.; Brawer, H.; Ramirez, A. P.; Ding, L.; Cao, H.; Liu, Q.; Dessau, D.; Ni, N. A van der Waals antiferromagnetic topological insulator with weak interlayer magnetic coupling. *Nat. Commun.* **2020**, 11 (1), 97.

22. Wu, J.; Liu, F.; Sasase, M.; Ienaga, K.; Obata, Y.; Yukawa, R.; Horiba, K.; Kumigashira, H.; Okuma, S.; Inoshita, T.; Hosono, H. Natural van der Waals heterostructural single crystals with both magnetic and topological properties. *Sci. Adv.* **2019**, *5* (11), eaax9989.
23. Hu, C.; Ding, L.; Gordon, K. N.; Ghosh, B.; Tien, H. J.; Li, H.; Linn, A. G.; Lien, S. W.; Huang, C. Y.; Mackey, S.; Liu, J.; Reddy, P. V. S.; Singh, B.; Agarwal, A.; Bansil, A.; Song, M.; Li, D.; Xu, S. Y.; Lin, H.; Cao, H.; Chang, T. R.; Dessau, D.; Ni, N. Realization of an intrinsic ferromagnetic topological state in $\text{MnBi}_8\text{Te}_{13}$. *Sci. Adv.* **2020**, *6* (30), eaba4275.
24. Tian, S.; Gao, S.; Nie, S.; Qian, Y.; Gong, C.; Fu, Y.; Li, H.; Fan, W.; Zhang, P.; Kondo, T.; Shin, S.; Adell, J.; Fedderwitz, H.; Ding, H.; Wang, Z.; Qian, T.; Lei, H. Magnetic topological insulator $\text{MnBi}_6\text{Te}_{10}$ with a zero-field ferromagnetic state and gapped Dirac surface states. *Phys. Rev. B* **2020**, *102* (3), 035144.
25. Wu, X.; Li, J.; Ma, X.-M.; Zhang, Y.; Liu, Y.; Zhou, C.-S.; Shao, J.; Wang, Q.; Hao, Y.-J.; Feng, Y.; Schwier, E. F.; Kumar, S.; Sun, H.; Liu, P.; Shimada, K.; Miyamoto, K.; Okuda, T.; Wang, K.; Xie, M.; Chen, C.; Liu, Q.; Liu, C.; Zhao, Y. Distinct Topological Surface States on the Two Terminations of MnBi_4Te_7 . *Physical Review X* **2020**, *10* (3), 031013.
26. Lapano, J.; Nuckols, L.; Mazza, A. R.; Pai, Y.-Y.; Zhang, J.; Lawrie, B.; Moore, R. G.; Eres, G.; Lee, H. N.; Du, M.-H.; Ward, T. Z.; Lee, J. S.; Weber, W. J.; Zhang, Y.; Brahlek, M. Adsorption-controlled growth of $\text{MnTe}(\text{Bi}_2\text{Te}_3)_n$ by molecular beam epitaxy exhibiting stoichiometry-controlled magnetism. *Phys. Rev. Mater.* **2020**, *4* (11), 111201(R).
27. Ou, Y.; Liu, C.; Zhang, L.; Feng, Y.; Jiang, G.; Zhao, D.; Zang, Y.; Zhang, Q.; Gu, L.; Wang, Y.; He, K.; Ma, X.; Xue, Q.-K. Heavily Cr-doped $(\text{Bi,Sb})_2\text{Te}_3$ as a ferromagnetic insulator with electrically tunable conductivity. *APL Materials* **2016**, *4* (8), 086101.

28. Wang, F.; Zhao, Y. F.; Yan, Z. J.; Zhuo, D.; Yi, H.; Yuan, W.; Zhou, L.; Zhao, W.; Chan, M. H. W.; Chang, C. Z. Evolution of Dopant-Concentration-Induced Magnetic Exchange Interaction in Topological Insulator Thin Films. *Nano Lett.* **2023**, 23 (7), 2483-2489.
29. Kou, X.; Lang, M.; Fan, Y.; Jiang, Y.; Nie, T.; Zhang, J.; Jiang, W.; Wang, Y.; Yao, Y.; He, L.; Wang, K. L. Interplay between different magnetisms in Cr-doped topological insulators. *ACS Nano* **2013**, 7 (10), 9205-9212.
30. Islam, F.; Lee, Y.; Pajerowski, D. M.; Oh, J.; Tian, W.; Zhou, L.; Yan, J.; Ke, L.; McQueeney, R. J.; Vaknin, D. Role of Magnetic Defects in Tuning Ground States of Magnetic Topological Insulators. *Adv. Mater.* **2023**, 35 (21), e2209951.
31. Xu, X.; Yang, S.; Wang, H.; Guzman, R.; Gao, Y.; Zhu, Y.; Peng, Y.; Zang, Z.; Xi, M.; Tian, S.; Li, Y.; Lei, H.; Luo, Z.; Yang, J.; Wang, Y.; Xia, T.; Zhou, W.; Huang, Y.; Ye, Y. Ferromagnetic-antiferromagnetic coexisting ground state and exchange bias effects in MnBi_4Te_7 and $\text{MnBi}_6\text{Te}_{10}$. *Nat. Commun.* **2022**, 13 (1), 7646.
32. Liu, Y.; Wang, L.-L.; Zheng, Q.; Huang, Z.; Wang, X.; Chi, M.; Wu, Y.; Chakoumakos, B. C.; McGuire, M. A.; Sales, B. C.; Wu, W.; Yan, J. Site Mixing for Engineering Magnetic Topological Insulators. *Physical Review X* **2021**, 11 (2), 021033.
33. Hu, C.; Lien, S.-W.; Feng, E.; Mackey, S.; Tien, H.-J.; Mazin, I. I.; Cao, H.; Chang, T.-R.; Ni, N. Tuning magnetism and band topology through antisite defects in Sb-doped MnBi_4Te_7 . *Phys. Rev. B* **2021**, 104 (5), 054422.
34. Zang, Z.; Zhu, Y.; Xi, M.; Tian, S.; Wang, T.; Gu, P.; Peng, Y.; Yang, S.; Xu, X.; Li, Y.; Han, B.; Liu, L.; Wang, Y.; Gao, P.; Yang, J.; Lei, H.; Huang, Y.; Ye, Y. Layer-Number-Dependent Antiferromagnetic and Ferromagnetic Behavior in MnSb_2Te_4 . *Phys. Rev. Lett.* **2022**, 128 (1), 017201.

35. Ge, W.; Sass, P. M.; Yan, J.; Lee, S. H.; Mao, Z.; Wu, W. Direct evidence of ferromagnetism in MnSb_2Te_4 . *Phys. Rev. B* **2021**, 103 (13), 134403.
36. Wimmer, S.; Sanchez-Barriga, J.; Kupperts, P.; Ney, A.; Schierle, E.; Freyse, F.; Caha, O.; Michalicka, J.; Liebmann, M.; Primetzhofer, D.; Hoffman, M.; Ernst, A.; Otrokov, M. M.; Bihlmayer, G.; Weschke, E.; Lake, B.; Chulkov, E. V.; Morgenstern, M.; Bauer, G.; Springholz, G.; Rader, O. Mn-Rich MnSb_2Te_4 : A Topological Insulator with Magnetic Gap Closing at High Curie Temperatures of 45-50 K. *Adv. Mater.* **2021**, 33 (42), e2102935.
37. Frolov, A. S.; Usachov, D. Y.; Fedorov, A. V.; Vilkov, O. Y.; Golyashov, V.; Tereshchenko, O. E.; Bogomyakov, A. S.; Kokh, K.; Muntwiler, M.; Amati, M.; Gregoratti, L.; Sirotina, A. P.; Abakumov, A. M.; Sanchez-Barriga, J.; Yashina, L. V. Ferromagnetic Layers in a Topological Insulator $(\text{Bi,Sb})_2\text{Te}_3$ Crystal Doped with Mn. *ACS Nano* **2022**, 16 (12), 20831-20841.
38. Mazza, A. R.; Lapano, J.; Meyerlii, H. M.; Nelson, C. T.; Smith, T.; Pai, Y. Y.; Noordhoek, K.; Lawrie, B. J.; Charlton, T. R.; Moore, R. G.; Ward, T. Z.; Du, M. H.; Eres, G.; Brahlek, M. Surface-Driven Evolution of the Anomalous Hall Effect in Magnetic Topological Insulator MnBi_2Te_4 Thin Films. *Adv. Funct. Mater.* **2022**, 32 (28), 2202234.
39. Brahlek, M.; Lapano, J.; Lee, J. S. Topological materials by molecular beam epitaxy. *J. Appl. Phys.* **2020**, 128 (21), 210902.
40. Yao, X.; Yi, H. T.; Jain, D.; Han, M. G.; Oh, S. Spacer-Layer-Tunable Magnetism and High-Field Topological Hall Effect in Topological Insulator Heterostructures. *Nano Lett.* **2021**, 21 (14), 5914-5919.
41. Chen, P.; Yao, Q.; Xu, J.; Sun, Q.; Grutter, A. J.; Quarterman, P.; Balakrishnan, P. P.; Kinane, C. J.; Caruana, A. J.; Langridge, S.; Li, A.; Achinuq, B.; Heppell, E.; Ji, Y.; Liu, S.; Cui, B.; Liu, J.; Huang, P.; Liu, Z.; Yu, G.; Xiu, F.; Hesjedal, T.; Zou, J.; Han, X.; Zhang, H.; Yang, Y.; Kou,

X. Tailoring the magnetic exchange interaction in MnBi_2Te_4 superlattices via the intercalation of ferromagnetic layers. *Nature Electronics* **2023**, 6, 18-27.

42. Watanabe, R.; Yoshimi, R.; Kawamura, M.; Kaneko, Y.; Takahashi, K. S.; Tsukazaki, A.; Kawasaki, M.; Tokura, Y. Enhancement of anomalous Hall effect in epitaxial thin films of intrinsic magnetic topological insulator MnBi_2Te_4 with Fermi-level tuning. *Appl. Phys. Lett.* **2022**, 120 (3), 031901.

43. Gong, Y.; Guo, J.; Li, J.; Zhu, K.; Liao, M.; Liu, X.; Zhang, Q.; Gu, L.; Tang, L.; Feng, X.; Zhang, D.; Li, W.; Song, C.; Wang, L.; Yu, P.; Chen, X.; Wang, Y.; Yao, H.; Duan, W.; Xu, Y.; Zhang, S.-C.; Ma, X.; Xue, Q.-K.; He, K. Experimental Realization of an Intrinsic Magnetic Topological Insulator. *Chinese Physics Letters* **2019**, 36 (7), 076801.

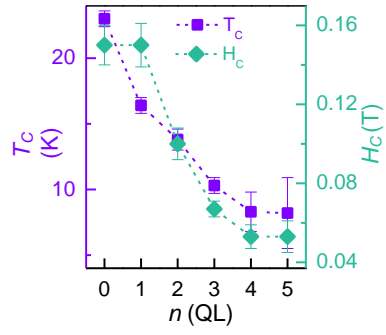
44. Chen, P.; Zhang, Y.; Yao, Q.; Tian, F.; Li, L.; Qi, Z.; Liu, X.; Liao, L.; Song, C.; Wang, J.; Xia, J.; Li, G.; Burn, D. M.; van der Laan, G.; Hesjedal, T.; Zhang, S.; Kou, X. Tailoring the Hybrid Anomalous Hall Response in Engineered Magnetic Topological Insulator Heterostructures. *Nano Lett.* **2020**, 20 (3), 1731-1737.

45. He, H. T.; Wang, G.; Zhang, T.; Sou, I. K.; Wong, G. K.; Wang, J. N.; Lu, H. Z.; Shen, S. Q.; Zhang, F. C. Impurity effect on weak antilocalization in the topological insulator Bi_2Te_3 . *Phys. Rev. Lett.* **2011**, 106 (16), 166805.

46. Li, Q.; Di Bernardo, I.; Maniatis, J.; McEwen, D.; Dominguez-Celorio, A.; Bhuiyan, M. T. H.; Zhao, M.; Tadich, A.; Watson, L.; Lowe, B.; Vu, T. H. Y.; Trang, C. X.; Hwang, J.; Mo, S. K.; Fuhrer, M. S.; Edmonds, M. T. Imaging the Breakdown and Restoration of Topological Protection in Magnetic Topological Insulator MnBi_2Te_4 . *Adv. Mater.* **2024**, 36 (24), 2312004.

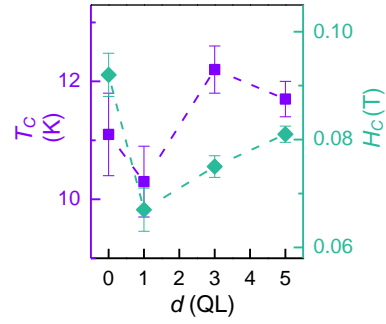
47. Yao, X.; Brahlek, M.; Yi, H. T.; Jain, D.; Mazza, A. R.; Han, M. G.; Oh, S. Hybrid Symmetry Epitaxy of the Superconducting Fe(Te,Se) Film on a Topological Insulator. *Nano Lett.* **2021**, 21 (15), 6518-6524.
48. Yao, X.; Mazza, A. R.; Han, M. G.; Yi, H. T.; Jain, D.; Brahlek, M.; Oh, S. Superconducting Fourfold Fe(Te,Se) Film on Sixfold Magnetic MnTe via Hybrid Symmetry Epitaxy. *Nano Lett.* **2022**, 22 (18), 7522-7526.
49. Yao, X.; Moon, J.; Cheong, S.-W.; Oh, S. Structurally and chemically compatible BiInSe₃ substrate for topological insulator thin films. *Nano Res.* **2020**, 13 (9), 2541-2545.
50. Kresse, G.; Furthmüller, J. Efficient iterative schemes for ab initio total-energy calculations using a plane-wave basis set. *Phys. Rev. B* **1996**, 54 (16), 11169-11186.
51. Kresse, G.; Joubert, D. From ultrasoft pseudopotentials to the projector augmented-wave method. *Phys. Rev. B* **1999**, 59 (3), 1758-1775.
52. Kresse, G.; Hafner, J. Ab initio molecular-dynamics simulation of the liquid-metal-amorphous-semiconductor transition in germanium. *Phys. Rev. B* **1994**, 49 (20), 14251-14269.
53. Kohn, W.; Sham, L. J. Self-Consistent Equations Including Exchange and Correlation Effects. *Phys. Rev.* **1965**, 140 (4A), A1133-A1138.

Bi ₂ Te ₃ (n QL)
MnBi ₂ Te ₄ (1 SL)
Bi ₂ Te ₃ (1 QL)
MnBi ₂ Te ₄ (1 SL)
Bi ₂ Te ₃ (n QL)



$2n + d = 7$

Bi ₂ Te ₃ (n QL)
MnBi ₂ Te ₄ (1 SL)
Bi ₂ Te ₃ (d QL)
MnBi ₂ Te ₄ (1 SL)
Bi ₂ Te ₃ (n QL)



TOC only